

PCCP

Accepted Manuscript



This is an *Accepted Manuscript*, which has been through the Royal Society of Chemistry peer review process and has been accepted for publication.

Accepted Manuscripts are published online shortly after acceptance, before technical editing, formatting and proof reading. Using this free service, authors can make their results available to the community, in citable form, before we publish the edited article. We will replace this *Accepted Manuscript* with the edited and formatted *Advance Article* as soon as it is available.

You can find more information about *Accepted Manuscripts* in the [Information for Authors](#).

Please note that technical editing may introduce minor changes to the text and/or graphics, which may alter content. The journal's standard [Terms & Conditions](#) and the [Ethical guidelines](#) still apply. In no event shall the Royal Society of Chemistry be held responsible for any errors or omissions in this *Accepted Manuscript* or any consequences arising from the use of any information it contains.

The effect of the zeolite pore size on the Lewis acid strength of extra-framework cations

HoViet Thang,^a Karel Frolich,^b Mariya Shamzhy,^c Pavla Eliášová,^c Miroslav Rubeš,^a Jiří Čejka,^c

Roman Bulánek,^b Petr Nachtigall^{a}*

^a Department of Physical and Macromolecular Chemistry, Faculty of Sciences, Charles University, Hlavova 8, 128 40 Prague 2, Czech Republic

^b Department of Physical Chemistry, Faculty of Chemical Technology, University of Pardubice, Studentska 573, 532 10 Pardubice, Czech Republic

^c J. Heyrovský Institute of Physical Chemistry, Academy of Sciences of the Czech Republic v.v.i., Dolejškova 3, 182 23 Prague 8, Czech Republic

Abstract

Catalytic activity and adsorption properties of zeolites depend on their topology and composition. For better understanding of the structure-activity relationship it is advantageous to focus just on one of these parameters. Zeolites synthesized recently by the ADOR protocol offer a new possibility to investigate the effect of the channel diameter on the adsorption and catalytic properties of zeolites: **UTL**, **OKO**, and **PCR** zeolites consist of the same dense 2D layers (IPC-1P) that are connected with different linkers (D4R, S4R, O-atom, respectively) resulting in the channel systems of different sizes (14Rx12R, 12Rx10R, 10Rx8R, respectively). Consequently,

extra-framework cation sites compensating charge of framework Al located in these dense 2D layers (channel-wall sites) are the same in all three zeolites. Therefore, the effect of the zeolite channel size on the Lewis properties of the cationic sites can be investigated independently on other factors determining the quality of Lewis sites. **UTL**, **OKO**, and **PCR** and pillared 2D IPC-1PI materials were prepared in Li-form and their properties were studied by a combination of experimental and theoretical methods. Qualitatively different conclusions are drawn for Li^+ located at the channel-wall sites and at the intersection sites (Li^+ located at the intersection of two zeolite channels): The Lewis acid strength of Li^+ at intersection sites is larger than that at channel-wall sites. The Lewis acid strength of Li^+ at channel-wall sites increases with decreasing channel size. When intersecting channels are small (10R \times 8R in **PCR**) the intersection Li^+ sites are no longer stable and Li^+ is preferentially located at the channel-wall sites. Last but not least, the increase in adsorption heats with the decreasing channel size (due to enlarged dispersion contribution) is clearly demonstrated.

1. Introduction

Adsorption and catalytic properties of zeolites depend on zeolite topology, chemical composition, and distribution of atoms (Si vs. Al) among different crystallographic sites.¹⁻⁶ Understanding of this seemingly simple dependence at the molecular level is complicated by the fact that individual effects are strongly coupled. For better understanding of the structure-activity relationship it is advantageous to focus just on a single effect. At the molecular level, adsorption and catalytic properties depend primarily on the coordination and accessibility of charge-balancing extra-framework cations (protons or metal cations).⁷⁻⁹ Information about the location and coordination of extra-framework cations for most zeolites cannot be directly obtained from experiment, instead it is often deduced from a combination of various experimental techniques¹⁰⁻¹² (see Ref. ¹³ for recent comprehensive review). A combination of experimental and

computational investigations has been shown to be particularly suitable for understanding of the extra-framework cation coordination in high-silica zeolites.¹⁴⁻²⁸

To understand the effects of the extra-framework cation coordination and the channel size on adsorption and catalytic properties of zeolites, a probe molecule, such as CO, has been used.²⁹⁻³¹ In high silica zeolites, the adsorption of CO is driven by two factors: by the effect from the bottom and by the effect from the top.^{32, 33} The effect from the bottom is due to the interaction of adsorbate with the primary extra-framework cation and it reflects the cation coordination with the framework; the stronger is the interaction of the extra-framework cation with the zeolite framework the weaker is the interaction with CO and lower adsorption heats and lower CO stretching vibrations ν_{CO} can be expected. The effect from the bottom is more pronounced for smaller cation such as Li^+ and Mg^{2+} .^{34, 35} Thus, the effect from the bottom reflects the Lewis acid strength of the extra-framework metal cation that is demonstrated by its ability to polarize an adsorbate. The effect from the top is due to the “secondary” interaction of adsorbed molecule with the zeolite framework in its vicinity. This effect is mostly due to the electrostatic and dispersion interactions and it leads to additional changes of CO stretching frequency. Experimentally observed characteristics of adsorbed probe molecules reflect both effects (from the top and from the bottom) simultaneously and individual effects can be demonstrated only computationally, using suitable models. A recent theoretical investigation of CO adsorption on 2D layered IPC-1PI and corresponding 3D **UTL** zeolites have shown that adsorption enthalpies and CO stretching frequencies are lower by 3 kJ mol⁻¹ and 5 cm⁻¹, respectively, in the 2D material (IPC-1P).³⁶

It has been recently shown that **UTL** zeolite can be converted into layered two-dimensional (2D) material IPC-1P by selective hydrolysis³⁷ and this 2D material can be further converted into new zeolites IPC-2 and IPC-4 (having **OKO** and **PCR** topology, respectively) via ADOR mechanism.³⁸⁻⁴⁰ The **OKO** zeolite was originally prepared via inverse sigma transformation;⁴¹ **OKO** and IPC-2 have the same framework connectivity but differ in the symmetry. A layered 2D material obtained upon the hydrolysis of **UTL** is denoted IPC-1P while the corresponding material obtained by pillaring is denoted IPC-1PI;

experimental results reported below were obtained on IPC-1PI while calculations were carried out for IPC-1P layers separated by vacuum (Section 2). We will use IPC-1PI to refer to pillared material (experimental and theoretical) while IPC-1P notation will denote the structure of 2D layers. These four materials (IPC-1PI, **UTL**, **OKO**, and **PCR**) thus constitute a unique set of adsorbents with the same dense 2D layers separated by different interlayer distances defined by different interlayer linkers. Consequently, these materials have different channel systems parallel to the 2D layer (Fig. 1). We denote these zeolites “IPC-1P group” since they all can be formally obtained from IPC-1P precursor. While the channel size increases from **PCR** to IPC-1PI, the structure remains relatively similar since parts of the channel defined by 2D layers do not change. Thus, the IPC-1P group represents a unique series where majority of extra-framework sites (those defined by dense 2D layers) are very similar, if not the same, and the differences in adsorption and catalytic properties must be related to the channel size. It gives us a unique opportunity to investigate the effect of the channel size without an influence of differences in the extra-framework coordination and improve our understanding of adsorption and catalytic processes taking place in zeolites. The results for such a unique series of zeolites with similar structures but increasing channel size are presented herein for the first time.

All four zeolites of IPC-1P group were prepared in the Li^+ form and the properties of extra-framework Li^+ sites were probed with the CO adsorbate. In addition to standard characterization techniques, the microcalorimetry and FTIR spectra were obtained from a zero coverage up to coverages greater than monolayer ($\text{CO}:\text{Li} > 1:1$). Experimental results are compared with computational results obtained for the same set of materials (results for Li-PCR and Li-OKO are presented herein while computational results for Li-IPC-1PI and Li-UTL are taken from Ref. ³⁶). Based on excellent agreement of theoretical and experimental data the effects of zeolite channel size on the Lewis acid strength (and thus the adsorption and catalytic activity) of extra-framework Li^+ sites are discussed.

2. Experimental and Computational methods

2.1. Synthesis and Characterization

Aluminogermanosilicate **UTL** and pure germanosilicate **UTL** were prepared according to a procedure described in the literature.⁴² For the synthesis of IPC-zeolites, **UTL** was used as the starting material and additional aluminium was incorporated during its hydrolysis as followed: calcined **UTL** (1 g) was hydrolysed in a mixture of solutions 1M CH₃COOH (150 ml) and 1M Al(NO₃)₃ (100 ml) at 90 °C for 16 hours. The product was isolated by filtration, washed with water and dried at 60 °C. For the synthesis of **OKO**, the hydrolysed sample (1g) was treated with 1M HNO₃ solution (10 g) and diethoxydimethylsilane Si(OCH₂CH₃)₂(CH₃)₂ (0.2 g). The reaction was performed in the autoclave under static conditions at 170° C for 16 hours. The final product was washed with water, dried at 60° C and finally calcined in the air flow at 750° C for 6 hours. For the synthesis of **PCR**, the hydrolysed sample was treated with neat octylamine at 80° C for 16 hours (with w/w ratio 1/13 g). The solid was then isolated by centrifugation and dried at the ambient temperature. The product was calcined in the air flow at 750° C for 8 h. For the synthesis of IPC-1PI, 1 g of hydrolysed sample was first swollen with 20 ml of 20 wt% cetyltrimethylammonium hydroxide solution (C₁₆TMA-OH) by stirring at ambient temperature for 16 hours. The IPC-1SW was then treated with TEOS (for 1g of zeolite 50 ml TEOS) at 85°C for 16 hours. The produced solid was hydrolysed in water and then calcined at 550°C for 6 hours.

The structure and crystallinity of zeolites were determined by X-ray powder diffraction using Bruker AXS D8 Advance diffractometer equipped with a graphite monochromator and a position sensitive detector Vântec-1 using CuK α radiation in Bragg–Brentano geometry.

Adsorption isotherms of nitrogen (at -196 °C) were measured on a Micromeritics ASAP 2020 static volumetric instrument. The BET area (S_{BET}) was evaluated by BET method using adsorption data in the p/p_0 range of 0.05-0.20. The adsorbed amount at relative pressure $p/p_0 = 0.98$ reflects the total adsorption capacity (V_{tot}). For adsorption isotherms of nitrogen, the t -plot method was applied to determine the volume of micropores (V_{micro}). Low-pressure adsorption isotherms of argon (at -186°C)

were measured on the same instrument in order to inspect pore-size distribution. Experimental data were treated by NL DFT model of Ar adsorption in H-zeolite at -186°C by SAIEUS software (Micromeritics).⁴³

The lithium forms of zeolites were obtained by an ion exchange in a 0.5 M aqueous solution of LiCl for two days at 35°C . After ion exchange, the samples were filtered and thoroughly washed by distilled water several times and finally dried at 120°C overnight. The crystallinity of Li-zeolites was checked by XRD. No decrease in crystallinity and no addition phase presence were observed in the XRD.

2.2. FT-IR spectroscopy of adsorbed CO

The samples were pressed into self-supporting wafers with density of 10 mg cm^{-2} and placed into home-made low temperature IR cell for transmission measurement. The zeolite samples were in situ activated (outgassed) in a dynamic vacuum (residual pressure $< 10^{-4}\text{ Pa}$) for 10 h at 430°C (with rate of temperature increase of $1^{\circ}\text{C min}^{-1}$ up to 130°C , then the sample was kept for 30 min at this temperature and subsequently temperature increased with the rate $5^{\circ}\text{C min}^{-1}$ up to 430°C). Infrared spectra (64 scans) were collected at temperature of liquid nitrogen with a resolution of 2 cm^{-1} on a Nicolet 6700 FTIR spectrometer equipped with an MCT/A cryodetector. Carbon monoxide (99.997 purity) used in the experiments was purified by a freeze-pump-thaw cycle. The CO adsorption on Li-zeolites was performed at equilibrium pressure of 0.1 Torr; CO pressure was then reduced until vibrational bands of adsorbed CO were detected (approximately 4 h). IR spectra of the surface CO complexes were collected each minute. The spectrum of dehydrated sample at temperature of liquid nitrogen recorded before CO adsorption was subtracted from each spectrum shown in this work.

2.3. Adsorption microcalorimetry

Prior to each calorimetric experiment, sample of the weight ca. 300 mg was outgassed by slowly increasing temperature with simultaneous careful evacuation up to residual pressure 10^{-4} Pa at 450 °C. The microcalorimetric/volumetric experiments were carried out using an isothermal Tian-Calvet type microcalorimeter (BT 2.15, SETARAM) combined with a homemade volumetric/manometric device equipped with capacitance pressure gauges (Pfeiffer Vacuum). The adsorption isotherms and heats of adsorption were measured at -100 °C by step-by-step introduction of CO (99.997 purity) into the cell. The system was equilibrated for 60 minutes for each dose and the equilibrium was monitored by both the pressure and the heat-flow measurements. The integral area of the peak in heat flow – time plot provided integral adsorption heat evolved at each adsorptive dose. The dependence of differential adsorption heat vs. adsorbed amount was obtained by numeric differentiation.

2.4. Models and Computational methods

The numbering scheme of framework atoms in **UTL**, **OKO**, and **PCR** structures is defined at the IZA database;⁴⁴ the use of three numbering schemes would make it complicated for a reader to follow the comparison of results for individual structure types. In fact, all three **UTL**, **OKO**, and **PCR** framework types are based on the same dense 2D layer (a material denoted IPC-1P)³⁷ and they differ only by a linker inter-connecting these 2D layers into 3D zeolites (O atom, S4R, and D4R for **PCR**, **OKO**, and **UTL**, respectively). Therefore, for comparison of all 3 framework types the **UTL** numbering scheme is adopted (Fig. 2) and the mapping with the IZA numbering is shown in Supplementary Materials (Table SI-1). The same numbering is used also for IPC-1PI layered material. To prevent the confusion with the IZA numbering the T-sites are denoted as T'-sites throughout this manuscript.

The notation of Li⁺ cation positions for all structures is shown in Fig. 2. Li⁺ positions located on the surface of channel wall (type I sites) can be classified as M_x and P_x, where M is the main (larger) channel and P is the perpendicular (smaller) channel, x is the size of the ring on the channel wall that hosts the extra-framework cation and I₂ stands for type II sites on the intersection (similar notation has

been introduced previously for other high-silica zeolites^{45, 46}). The substitution of Al for Si was investigated for all distinguishable T-sites except those located at the interlayer linker (S4R unit in **OKO**). For each investigated location of the framework Al the most energetically stable site of extra-framework Li⁺ cation was found and for these Li⁺ sites the adsorption of CO was considered.

Unit cell parameters previously determined for IPC-2 ($a=12.5162\text{\AA}$, $b=13.8880\text{\AA}$, $c=13.9682\text{\AA}$, and $\alpha=118.7520^\circ$, $\beta=90.1740^\circ$, $\gamma=107.0870^\circ$) and **PCR** ($a=20.3599\text{\AA}$, $b=14.1746\text{\AA}$, $c=12.4572\text{\AA}$, and $\alpha=\gamma=90^\circ$, $\beta=114.0905^\circ$) were adopted.³⁸ Since the methods used for the calculations on **OKO** and **PCR** zeolites are exactly the same as described previously for **UTL** and IPC-1PI,³⁶ they are only briefly summarized below. All calculations were performed at the DFT level using Perdew-Burke-Ernzerhof (PBE) exchange-correlation functional,^{47, 48} the projector augmented wave approximation (PAW)^{49, 50} and the plane wave basis set with a 400 eV kinetic energy cut-off. Brillouin-zone sampling was restricted to the Γ point. Calculations were performed with the VASP program package (version 5.3.3).^{51, 52} The structure optimizations were carried out with relaxed ions and a frozen unit cell. The zero point energies (ZPE) were calculated within the harmonic approximation, considering 6 degrees of freedom of CO. The standard enthalpies were reported at 0 K. CO stretching frequencies were calculated by $\nu_{\text{CO}}/r_{\text{CO}}$ correlation method described in Ref. ⁵³. The CO adsorption energies calculated at the PBE level were corrected for a missing dispersion contribution using the DFT/CC method.⁵⁴ Details of the method for Li-zeolites were described in Ref. ³⁶. Dispersion and local contributions (denoted Δ_{disp} and Δ_{local} , respectively) to the interaction energy were evaluated as well. The part of DFT/CC correction upon elimination the Li...C and Li...O correction is used for Δ_{disp} and interaction energy calculated at the PBE level is used for Δ_{local} . The IR spectra of adsorbed CO were modelled following the method described previously,⁵⁵ assuming statistical distribution of Al inside the dense 2D layers.

3. Experimental results

The X-ray diffraction patterns of **UTL**, **OKO**, **PCR**, and 2D IPC-1PI zeolites reported in Fig. 3a are in good agreement with those reported in the literature.^{37, 38} No diffraction lines of additional phases were observed in the diffraction patterns. Nitrogen adsorption isotherms (Fig. 3b) are characteristic of a microporous material lacking secondary mesopores, except the isotherm for IPC-1PI that is typical for mesoporous material. The Si/Al ratios, BET areas, total pore volumes, volumes of micropores, and pore sizes are reported in Table 1. The argon adsorption isotherms and pore-size distributions are shown in Supplementary Materials (Fig. SI-1).

3.1. FTIR spectra of CO adsorbed on OKO and PCR

The IR spectra of CO adsorbed on all four Li-zeolites at liquid nitrogen temperature are shown in the Fig. 4 and adsorption characteristics obtained for low coverages are summarized in Table 2. The spectra recorded on individual samples differ in a number and relative intensity of spectral bands. The IR spectra of CO adsorbed on Li-IPC-1PI (see Fig. 4a) are characterized by only one, relatively broad band with maximum at 2187 cm^{-1} . The band is clearly asymmetric on the low frequency side and its maximum shifts with increasing coverage to 2183 cm^{-1} . The spectra of CO adsorbed on Li-**UTL** (Fig. 4b) reveal two bands at 2194 and 2187 cm^{-1} . The relative intensity of bands changes with coverage. The high-frequency band dominates the spectra at low coverages and there is a shoulder at low-frequency side at about 2189 cm^{-1} . With increasing coverage, the low-frequency shoulder develops and becomes the dominant band. Simultaneously, the position of low frequency band slightly shifts from 2189 to 2187 cm^{-1} . IR spectra of the CO adsorbed on Li-**OKO** zeolite (Fig. 4c) resemble spectra obtained for Li-**UTL** zeolite. The spectra obtained for the lowest coverage show two well-distinguished bands at 2195 and 2188 cm^{-1} . The maxima of both bands are rather coverage independent, whereas relative intensities of these bands change. The band at 2188 cm^{-1} dominates the spectra recorded at the high coverage. Relative intensity of the high frequency band with respect to the low frequency one is higher in Li-**UTL** than in Li-**OKO** zeolite. The IR spectra of CO adsorbed on Li-**PCR** (Fig. 4d) are characterized by the single asymmetric absorption band occurring below 2190 cm^{-1} . At low coverage, the band is centered at 2188 cm^{-1} with half-width

around 7.5 cm^{-1} . With increasing coverage, the maximum of the band is shifted to 2186 cm^{-1} and the shoulder at around 2179 cm^{-1} is developed.

3.2. Adsorption microcalorimetry of CO adsorption on OKO and PCR

Calorimetric curves for the CO adsorption on investigated Li-zeolites and Li-IPC-1PI at $-100 \text{ }^\circ\text{C}$ are depicted in Fig. 5. The differential heat of adsorption is plotted as a function of sample coverage (CO:Li ratio equal to 1 is considered to be 100%). The decrease in the adsorption heat with coverage reflects significant adsorption heterogeneity (in terms of energy) for all studied materials. Li-IPC-1PI exhibits the lowest adsorption heats from all four samples. Calorimetric curve of Li-IPC-1PI starts at 34.5 kJ mol^{-1} and very slowly decreases to approximately 30 kJ mol^{-1} at 60% of coverage. Then the heat falls to 20 kJ mol^{-1} followed again by slow decrease to 17 kJ mol^{-1} , at which calorimetric curve levels-off. The adsorption heats on Li-UTL zeolite are higher compared to Li-IPC-1PI. The first CO doses (up to 15 % of coverage) result in heats of 41 kJ mol^{-1} , followed by a decrease to approximately 32 kJ mol^{-1} where distinct plateau is clearly visible. The heats start to slowly decrease at coverage higher than 75% and level off at 18 kJ mol^{-1} . The strongest adsorption sites in Li-OKO zeolite are characterized by 43 kJ mol^{-1} and the heat higher than 40 kJ mol^{-1} can be detected up to coverage of 30 %. Then the heat monotonically decreases to 20 kJ mol^{-1} at coverages above 100%. Adsorption of CO on Li-PCR zeolite exhibits the largest initial adsorption heat (44 kJ mol^{-1}) from all investigated materials. Subsequent increase in coverage is reflected by substantial decrease in the heats to approximately 30 kJ mol^{-1} at near 100% of coverage. It must be noted that heats of CO adsorption on Li-PCR is significantly lower compared to heats on Li-OKO at intermediate coverage.

4. Computational results

4.1. Li^+ cation sites in OKO and PCR

Following the previous investigation of Li^+ sites in UTL and IPC-1PI³⁶ the energetically preferable Li^+ sites located in the vicinity of each of 10 T-sites in OKO and PCR were investigated; Li-O_f distances are

summarized for all four materials in Supplementary Materials (Table SI-2). Both **OKO** and **PCR** zeolites reflect a strong preference of Li^+ cations in type I site on the channel wall (Table 3), similar to **FER**⁵⁶ and **MFI**⁵⁷. The Li^+ cation is located in type II site only in one and two cases in **PCR** and **OKO**, respectively (Table 3). Comparing the most stable Li^+ cation position in **OKO** and **PCR**, it is apparent that Li^+ cation positions and coordination number (CN) are the same in both materials when framework Al atom is in T3', T4', T5', T8', T9', and T11' (Fig. 2). Since these sites are clearly defined by 2D layer and they are not affected by the inter-layer linker they will be denoted "layer sites". On the contrary, when framework Al atom is in T6', T7', T10', and T12', both site type and coordination number change between **OKO** and **PCR**. These sites will be denoted "inter-layer sites"; note that such sites are not necessarily located in the inter-layer region, however, their relative stability (and thus populations) are affected by the inter-layer linkers.

4.2. CO adsorption in OKO and PCR

The adsorption energies and stretching frequencies of CO were calculated to evaluate Lewis acid strength of the most stable Li^+ cation site found for particular Al position. Characteristics of CO adsorption complexes on Li^+ sites in **OKO** and **PCR** are reported in Table 3 summarizing Li-O_f distances, adsorption enthalpies $\Delta H(0\text{ K})$, and CO stretching frequencies ν_{CO} . The sensitivity of CO probe molecule to the local environment is reflected in ν_{CO} and ΔH that ranges from 2178 to 2197 cm^{-1} and from -29 to -46 kJ mol^{-1} , respectively. Examples of CO adsorption complexes in **OKO** and **PCR** are shown in Fig. 6 together with corresponding adsorption complexes found previously³⁶ in **UTL** and **IPC-1PI**.

Correction of PBE interaction energies evaluated at the DFT/CC level accounts mostly for the lack of dispersion interactions; they are summarized in Supplementary Materials, Table SI-3. They are rather important in **PCR** (-16 kJ mol^{-1} on average) where they represent 30-50% of the overall interaction energy. This is due to a relatively small size of **PCR** channel system (intersecting 10R and 8R channels) where CO primarily bound to the Li^+ cation is within vdW radii of many framework atoms. Consequently, dispersion interactions do not depend on the cation site. Due to a larger diameter of **OKO**

channel system, dispersion contributions are smaller than in **PCR** (by about 5 kJ mol^{-1} on average) and larger dependence on particular Li^+ position in **PCR** can be observed. In the case of **OKO** zeolite, the dispersion corrections account for 20-30% of overall interaction energies. For *layer sites* (see above), adsorption enthalpies in **PCR** are $4\text{-}8 \text{ kJ mol}^{-1}$ larger than in **OKO**, that can be attributed mostly to the increased importance of dispersion interaction in **PCR** having a small channel system (effect from the top). Examples of corresponding CO adsorption complexes are shown in Fig. 6 for Al in T4' (Fig. 6a-6d), and T3' (Fig. 6e-6h). In the case of *inter-layer sites*, the situation is opposite – adsorption enthalpies in **OKO** are up to 12 kJ mol^{-1} larger than in **PCR** for corresponding adsorption sites (Table 3). This difference clearly results from the effect from the bottom; coordination of Li^+ is larger in **PCR** ($\text{CN} = 4$) than in **OKO** ($\text{CN} \leq 3$). For the same reason also ν_{CO} frequencies are larger in **OKO** than in **PCR** by $8\text{-}16 \text{ cm}^{-1}$. Examples of CO adsorption complexes are shown for Al located in T10' and in T7' sites in Fig. 6 6k-6l and Fig. 6o-6p, respectively.

5. Discussion

The experimental and theoretical results reported above for Li-**PCR** and Li-**OKO** zeolites are discussed first, followed by a broader discussion of the results obtained for the series of Li-exchanged IPC-1PI, **UTL**, **OKO**, and **PCR** zeolites.

5.1. CO adsorption on Li^+ sites: experiment vs. theory

Calculated CO stretching frequencies are in quantitative agreement with the band maxima obtained experimentally for CO adsorbed on Li-**OKO** (2195 and 2188 cm^{-1}) and on Li-**PCR** (2188 and shoulder at 2176 cm^{-1}), thus, experimental spectra can be straightforwardly interpreted based on the theoretical investigation. The high-frequency band at 2195 cm^{-1} observed for CO/Li-**OKO** is due to the CO adsorption on two-coordinated I2 sites (Table 2 and Fig. 4). CO adsorption complexes on all other Li^+ sites (with 3- or 4-fold coordination) in Li-**OKO** are characterized by ν_{CO} between 2181 and 2191 cm^{-1} , well within the experimentally observed band centered at 2188 cm^{-1} . Larger values of $-\Delta H$ found for two-

coordinated sites explain the relative intensity of two bands reported for CO/Li-**OKO** in Fig. 4c. As for Li-**PCR**, in agreement with experimental data (Fig. 4d) no high-frequency CO adsorption sites (above 2190 cm^{-1}) were found (Table 3). Even the adsorption complex formed on I2 site is characterized by $\nu_{\text{CO}} = 2187\text{ cm}^{-1}$, that is 8 cm^{-1} lower than the one found for corresponding adsorption complex in Li-**OKO**. Note that Li^+ in I2 site in Li-**PCR** is actually located inside the 8R window of the channel; therefore, CO adsorption complex is almost perpendicular to Al—Si direction (Fig. 6d). CO adsorption complexes on *layer sites* (ν_{CO} between $2186\text{--}2190\text{ cm}^{-1}$) are characterized by higher $-\Delta H$ values than complexes on *inter-layer sites* (ν_{CO} between $2178\text{--}2181\text{ cm}^{-1}$); that explains why the band maximum is shifted and shoulder is formed at higher CO coverage. Experimental and calculated adsorption heats are in good agreement as well: at low CO coverage there are stronger adsorption sites on Li-**PCR** than on Li-**OKO** while at the coverage approaching $\text{CO}/\text{Li}^+ = 1$ the Li-**OKO** zeolite shows stronger adsorption sites than Li-**PCR** (Table 3). This is in line with experimental data (Fig. 5). Even quantitative agreement is reasonable – estimated experimental adsorption heats at zero coverage (43 and 44 kJ mol^{-1} for Li-**OKO** and Li-**PCR**, respectively) are close to values reported for the low-coordinated Li^+ sites (Table 2). Computational results reported previously for Li-IPC-1PI and Li-UTL³⁶ are compared with experimental results reported above in Table 2. A good qualitative and quantitative agreement between experimental and theoretical results reported above entitles us to discuss the subtle details of extra-framework cation coordination in a series of materials with similar topologies but different pore sizes.

5.2. Li^+ coordination and Lewis acid strength vs. pore dimension

Results reported above for Li-IPC-1PI, Li-UTL, Li-**OKO**, and Li-**PCR** may give us new insight on how the pore diameter affects the coordination of extra-framework cations and how that affects their Lewis acid strength. The structures of all four materials discussed here consist of identical 2D dense layers that are interconnected differently into 3D materials (Fig. 1): (i) IPC-1PI pillared material contains 2D IPC-1P layers (containing framework Al and thus extra-framework cations); the void space above the adsorption site is large compared to the size of the adsorbate and adsorption on Li-IPC-1PI can be viewed

as an adsorption on thin 2D IPC-1P layer. (ii) IPC-1P layers in **UTL** are connected by D4R units, forming relatively large 14R and 12R interconnected channels. (iii) Connection of IPC-1P layers with S4R, zeolite **OKO**, results in 12R x 10R channel system. (iv) Direct condensation of IPC-1P layers (linked simply by oxygen atoms) gives **PCR** zeolite with 10R x 8R channels. While these four materials differ in the pore size (decreasing in the order IPC-1PI > **UTL** > **OKO** > **PCR**) they have very similar topology – *layer sites* defined above (Al in T3', T4', T5', T8', T9', T11') are not much effected by the inter-layer linking and they are expected to be very similar in all four systems. On the contrary, *inter-layer sites* (T6' and T7' – adjacent T-atoms to inter-layer linker; T10' and T12' – bridging T6' and T7' T-sites) depends on the way how IPC-1P layers are linked together and they are expected to have different properties. Computational results for all four materials are summarized in Supplementary Materials; Li⁺ coordination and dispersion contribution to CO interaction with zeolite are reported in Tables SI-2 and SI-3, respectively. Characteristics of CO adsorption complexes are summarized in Table 4.

First, we focus the discussion on *layer sites*. The coordination of Li⁺ cations for particular *layer site* (defined by Al position) is the same in all four materials inspected herein and even Li-O distances are very similar (cf. Table SI-2). Therefore, any differences along the IPC-1PI – **UTL** – **OKO** – **PCR** series found for *layer sites* must be due to the changes in channel diameter and its curvature. Averaged values of corresponding adsorption characteristics are reported in Table 5. Adsorption enthalpies increase for *layer sites* in order IPC-1PI < **UTL** < **OKO** < **PCR**. Inspection of the dispersion contribution (obtained from the DFT/CC correction) and of the local contribution (PBE part of an overall interaction) reveals that the average dispersion interactions for *layer sites* are the same for IPC-1PI, **UTL**, and **OKO** (-11 kJ mol⁻¹) while they are larger (-16 kJ mol⁻¹) for **PCR**. It follows that the Lewis acid strength of Li⁺ cations which can be roughly quantified by Δ_{local} increases with the decreasing diameter of channels (Table 5). This is also apparent from Fig. 7 that summarizes adsorption enthalpies and ν_{CO} for all four materials.

The CO stretching frequency is determined by a combination of the effect from the bottom and the effect from the top.^{32, 33} The effect from the bottom is represented by cation Lewis acid strength (its ability to polarize an adsorbate) – ν_{CO} increases with increasing cation Lewis acid strength. The effect

from the top also leads to the ν_{CO} increase when the channel becomes smaller and CO vibrates “against” the wall. Following this model, ν_{CO} increases from IPC-1PI to **UTL** to **OKO** (Tables 5); however, ν_{CO} calculated for **PCR** does not increase with respect to zeolites with larger pores. This unexpected frequency decrease found for *layer sites* in **PCR** is in agreement with experimental observation (Fig. 4 and Table 2) and it is similar to the situation found previously for Li-**MFI** and Li-**FER** zeolites (having 10R x 10R and 10R x 8R intersecting channel systems, respectively).^{34, 58, 59}

As for the *inter-layer sites* the coordination of Li^+ changes from system to system (Table SI-2). Therefore, there are significantly larger differences between cation characteristics (Table 5). Intersection I2 sites, where Li^+ is coordinated to only 2 framework oxygens, exist only in Li-**UTL** and Li-**OKO**; CO adsorption complexes on these I2 sites show the highest frequency (2196-97 cm^{-1}), in agreement with experiment (Fig. 4). In the case of Li-**PCR**, the Li^+ in *inter-layer sites* is always coordinated to four framework oxygen atoms (Table 3) and consequently its Lewis acid strength is rather small (Table 5). It follows that both $-\Delta H$ and ν_{CO} values are significantly lower than in the case of **UTL** and **OKO**. The *inter-layer sites* in Li-IPC-1PI have the lowest Lewis acid strength reflected in low $-\Delta H$ and ν_{CO} values. First, there are no channels and intersections in Li-IPC-1PI, second, a smaller rigidity of 2D zeolite (compared to 3D one) results in better accommodation of Li^+ by framework atoms.³⁶

The analysis presented above can be summarized on the example of experimental IR spectra of CO on all four materials presented in Fig. 4. The high frequency bands at 2194 cm^{-1} observed only for Li-**UTL** and Li-**OKO** are due to the presence of Li^+ cations in the intersection I2 sites. These sites do not exist in Li-**PCR** where Li^+ preferentially binds at channel wall sites and these sites cannot exist in layered Li-IPC-1PI. The low energy bands experimentally observed at 2183, 2187, 2187, and 2186 cm^{-1} for Li-IPC-1PI, Li-**UTL**, Li-**OKO**, and Li-**PCR**, respectively, correspond to CO adsorbed on channel wall sites where Li^+ is coordinated to at least three framework oxygen atoms. Relatively small differences in band maxima positions are due to the changes in Lewis acid strength of Li^+ sites. The band shoulders observed for Li-**PCR** and Li-IPC-1PI at about 2176 cm^{-1} are mostly due to Li^+ in *inter-layer sites* which are formed

in place of intersection sites in **OKO** and **UTL**. Thus, the strongest adsorption Li^+ sites in Li-**UTL** and Li-**OKO** becomes the weakest adsorption sites in Li-**PCR** and Li-**IPC-1PI**.

The results reported for three Li-zeolites and one structurally related Li-pillared material possessing the same structure of the layers clearly show that the correlation between $-\Delta H$ and ν_{CO} is rather weak.¹³ Such correlation can only exist if both $-\Delta H$ and ν_{CO} are determined by the effect from the bottom and the effect from the top is negligible or constant. However, this is not the case as can be nicely demonstrated on the example of Li-**PCR** zeolite: large adsorption enthalpy is due to a significant dispersion contribution (CO fits well in 10R x 8R channel system) and it does not correspond to lower values of ν_{CO} .

Adsorption enthalpies were calculated at the DFT/CC level,⁵⁴ using correction functions derived previously.³⁶ Very good agreement between calculated and experimental adsorption heats was found for all four Li-exchanged materials investigated here. This agreement confirms that common DFT functionals overestimate interaction between the CO molecule and Li (alkali metals in general) cation and good agreement with experiment can only be achieved upon appropriate correction. Adsorption enthalpies calculated at the PBE-D3 level at PBE optimized geometries for Li-**PCR** were as large as -50 kJ mol^{-1} ; this overestimation is mostly due to the overestimation of $\text{Li}^+ \dots \text{CO}$ interaction.

6. Conclusions

Lewis acidity of alkali-exchanged zeolites is determined by the Lewis acid strength of individual extra-framework cation sites. The Lewis acid strength depends on cation coordination – the weaker is the interaction between the extra-framework cation and zeolite framework and more accessible is this cation the stronger is its Lewis acid strength. Therefore, cations located at the intersection of two channels are more active in adsorption and catalysis driven by the Lewis acidity than cations located inside the channels at the so-called channel-wall sites. The details of Lewis acid strength of Li-exchanged zeolites have been investigated by a combination of experimental (FTIR and microcalorimetry) and computational (DFT/CC and ω/r) methods using a CO probe molecule.

A unique series of zeolites with the same dense 2D layers with different interlayer linkers (**IPC-1PI**, **UTL**, **OKO**, and **PCR**) has been investigated. Majority of Li^+ sites defined by framework Al in the 2D layer have identical local environment in all investigated materials. Therefore, the differences between them can be attributed to the size of the channels parallel to the 2D layers. A very good agreement between calculated and experimental adsorption enthalpies and CO stretching frequencies entitles us to draw following conclusions:

- (i) The highest Lewis acid strength has been found for Li^+ cation coordinated to only two framework oxygen atoms at the intersection of two channels where Li^+ cation is located at the void space of the intersection. Such sites can only exist on the intersection of channels of the sizes larger than 8R – they only exist in Li-**UTL** and Li-**OKO** (having 14Rx12R and 12Rx10R channel systems, respectively). Intersection sites do not exist in Li-**PCR** (intersection of 10R and 8R channels) and they cannot exist in IPC-1PI. Thus, Li-**UTL** and Li-**OKO** have the strongest Lewis acid sites.
- (ii) Evaluation of Lewis acid strength based on adsorption heats could be misleading; apart from (mostly electrostatic) interaction with the extra-framework cation there is a significant contribution from dispersion interactions between adsorbate and zeolite framework. Due to good “fit” of CO into the 10Rx8R channel system of Li-**PCR** the dispersion component for this system is significantly larger than for other investigated zeolites and the largest adsorption heats were measured (and calculated) for Li-**PCR**, despite the fact that there are no sites with large Lewis acid strength at the channel intersection.
- (iii) A detail analysis of Li^+ sites defined by 2D dense layers shows that Lewis acid strength depends on the channel dimension: Li^+ cations in smaller channels show slightly larger Lewis acid strength.

Acknowledgement:

This work was supported by the Czech Science Foundation Grant No. P106/12/G015 (Centre of Excellence). Computational resources were provided by MetaCentrum under the program LM2010005 and the CERIT-SC under the program Centre CERIT Scientific Cloud, part of the Operational Program Research and Development for Innovations, Reg.no. CZ.1.05/3.2.00/08.0144.

References

1. D. Barthomeuf, *Mater. Chem. Phys.*, 1987, **17**, 49-71.
2. J. D. Rimer, M. Kumar, R. Li, A. I. Lupulescu and M. D. Oleksiak, *Catal. Sci. Technol.*, 2014, **4**, 3762-3771.
3. S. Bordiga, C. Lamberti, F. Geobaldo, A. Zecchina, G. T. Palomino and C. O. Arean, *Langmuir*, 1995, **11**, 527-533.
4. L. Grajciar, J. Cejka, A. Zupal, C. Otero Arean, G. Turnes Palomino and P. Nachtigall, *Chemsuschem*, 2012, **5**, 2011-2022.
5. P. Y. Dapsens, C. Mondelli and J. Perez-Ramirez, *Chem. Soc. Rev.*, 2015, **44**, 7025-7043.
6. T. Mori, A. Itadani, E. Tabuchi, Y. Sogo, R. Kumashiro, M. Nagao and Y. Kuroda, *Phys. Chem. Chem. Phys.*, 2008, **10**, 1203-1212.
7. H. Knozinger and S. Huber, *J. Chem. Soc. Faraday Trans.*, 1998, **94**, 2047-2059.
8. K. Hadjiivanov, in *Adv. Catal.*, Vol 57, ed. F. C. Jentoft, 2014, vol. 57, pp. 99-318.
9. I. Salla, T. Montanari, P. Salagre, Y. Cesteros and G. Busca, *Phys. Chem. Chem. Phys.*, 2005, **7**, 2526-2533.
10. V. V. Tersikh, C. I. Ratcliffe, J. A. Ripmeester, C. J. Reinhold, P. A. Anderson and P. P. Edwards, *J. Am. Chem. Soc.*, 2004, **126**, 11350-11359.
11. T. Yumura, H. Yamashita, H. Torigoe, H. Kobayashi and Y. Kuroda, *Phys. Chem. Chem. Phys.*, 2010, **12**, 2392-2400.
12. H. Yamashita, M. Matsuoka, K. Tsuji, Y. Shioya, M. Anpo and M. Che, *J. Phys. Chem.*, 1996, **100**, 397-402.
13. S. Bordiga, C. Lamberti, F. Bonino, A. Travert and F. Thibault-Starzyk, *Chem. Soc. Rev.*, 2015, **44**, 7262-7341.
14. B. Bonelli, B. Civalieri, B. Fubini, P. Ugliengo, C. O. Arean and E. Garrone, *J. Phys. Chem. B*, 2000, **104**, 10978-10988.
15. B. Civalieri, A. M. Ferrari, M. Lluell, R. Orlando, M. Merawa and P. Ugliengo, *Chem. Mater.*, 2003, **15**, 3996-4004.
16. P. Nachtigall, M. Davidova and D. Nachtigallova, *J. Phys. Chem. B*, 2001, **105**, 3510-3517.
17. C. O. Arean, M. R. Delgado, K. Frolich, R. Bulanek, A. Pulido, G. F. Bibiloni and P. Nachtigall, *J. Phys. Chem. C*, 2008, **112**, 4658-4666.
18. M. Fischer, M. Rodriguez Delgado, C. Otero Arean and C. Oliver Duran, *Theor. Chem. Acc.*, 2015, **134**.
19. G. N. Vayssilov, M. Staufer, T. Belling, K. M. Neyman, H. Knozinger and N. Rosch, *J. Phys. Chem. B*, 1999, **103**, 7920-7928.

20. E. A. Pidko, J. Xu, B. L. Mojet, L. Lefferts, I. R. Subbotina, V. B. Kazansky and R. A. vanSanten, *J. Phys. Chem. B*, 2006, **110**, 22618-22627.
21. A. Itadani, T. Yumura, T. Ohkubo, H. Kobayashi and Y. Kuroda, *Phys. Chem. Chem. Phys.*, 2010, **12**, 6455-6465.
22. P. Rejmak, E. Broclawik, K. Gora-Marek, M. Radon and J. Datka, *J. Phys. Chem. C*, 2008, **112**, 17998-18010.
23. C. Busco, V. Bolis and P. Ugliengo, *J. Phys. Chem. C*, 2007, **111**, 5561-5567.
24. C. Busco, A. Barbaglia, M. Broyer, V. Bolis, G. M. Foddanu and P. Ugliengo, *Thermochim. Acta*, 2004, **418**, 3-9.
25. V. Van Speybroeck, K. Hemelsoet, L. Joos, M. Waroquier, R. G. Bell and C. R. A. Catlow, *Chem. Soc. Rev.*, 2015, **44**, 7044-7111.
26. R. Kumashiro, K. Fujie, A. Kondo, T. Mori, M. Nagao, H. Kobayashi and Y. Kuroda, *Phys. Chem. Chem. Phys.*, 2009, **11**, 5041-5051.
27. P. Y. Storozhev, C. O. Arean, E. Garrone, P. Ugliengo, V. A. Ermoshin and A. A. Tsyganenko, *Chem. Phys. Lett.*, 2003, **374**, 439-445.
28. P. Ugliengo, E. Garrone, A. M. Ferrari, A. Zecchina and C. O. Arean, *J. Phys. Chem. B*, 1999, **103**, 4839-4846.
29. A. Zecchina and C. O. Arean, *Chem. Soc. Rev.*, 1996, **25**, 187-&.
30. K. I. Hadjiivanov and G. N. Vayssilov, in *Adv. Catal.*, Vol 47, eds. B. C. Gates and H. Knozinger, 2002, vol. 47, pp. 307-511.
31. P. Ugliengo, C. Busco, B. Civalieri and C. M. Zicovich-Wilson, *Mol. Phys.*, 2005, **103**, 2559-2571.
32. D. Nachtigallova, O. Bludsky, C. O. Arean, R. Bulanek and P. Nachtigall, *Phys. Chem. Chem. Phys.*, 2006, **8**, 4849-4852.
33. C. O. Arean, M. R. Delgado, C. L. Bauca, L. Vrbka and P. Nachtigall, *Phys. Chem. Chem. Phys.*, 2007, **9**, 4657-4661.
34. P. Nachtigall, K. Frolich, H. Drobna, O. Bludsky, D. Nachtigallova and R. Bulanek, *J. Phys. Chem. C*, 2007, **111**, 11353-11362.
35. R. Bulanek, I. Voleska, E. Ivanova, K. Hadjiivanov and P. Nachtigall, *J. Phys. Chem. C*, 2009, **113**, 11066-11076.
36. H. V. Thang, M. Rubes, O. Bludsky and P. Nachtigall, *J. Phys. Chem. A*, 2014, **118**, 7526-7534.
37. W. J. Roth, O. V. Shvets, M. Shamzhy, P. Chlubna, M. Kubu, P. Nachtigall and J. Cejka, *J. Am. Chem. Soc.*, 2011, **133**, 6130-6133.
38. W. J. Roth, P. Nachtigall, R. E. Morris, P. S. Wheatley, V. R. Seymour, S. E. Ashbrook, P. Chlubna, L. Grajciar, M. Polozij, A. Zukal, O. Shvets and J. Cejka, *Nat. Chem.*, 2013, **5**, 628-633.
39. P. Eliasova, M. Opanasenko, P. S. Wheatley, M. Shamzhy, M. Mazur, P. Nachtigall, W. J. Roth, R. E. Morris and J. Cejka, *Chem. Soc. Rev.*, 2015, **44**, 7177-7206.
40. M. Mazur, P. S. Wheatley, M. Navarro, W. J. Roth, M. Položij, A. Mayoral, P. Eliášová, P. Nachtigall, J. Čejka and R. E. Morris, *Nat. Chem.*, 2016, **8**, 58-62.
41. E. Verheyen, L. Joos, K. Van Havenbergh, E. Breynaert, N. Kasian, E. Gobechiya, K. Houthoofd, C. Martineau, M. Hinterstein, F. Taulelle, V. Van Speybroeck, M. Waroquier, S. Bals, G. Van Tendeloo, C. E. A. Kirschhock and J. A. Martens, *Nat. Mater.*, 2012, **11**, 1059-1064.
42. M. V. Shamzhy, O. V. Shvets, M. V. Opanasenko, P. S. Yaremov, L. G. Sarkisyan, P. Chlubna, A. Zukal, V. R. Marthala, M. Hartmann and J. Cejka, *J. Mater. Chem.*, 2012, **22**, 15793-15803.
43. J. Jagiello, *Langmuir*, 1994, **10**, 2778-2785.
44. C. Baerlocher and L. B. McCusker, (<http://www.iza-structure.org/databases/>).
45. D. Nachtigallova, P. Nachtigall, M. Sierka and J. Sauer, *Phys. Chem. Chem. Phys.*, 1999, **1**, 2019-2026.

46. O. Bludsky, M. Silhan, P. Nachtigall, T. Bucko, L. Benco and J. Hafner, *J. Phys. Chem. B*, 2005, **109**, 9631-9638.
47. J. P. Perdew, K. Burke and M. Ernzerhof, *Phys. Rev. Lett.*, 1996, **77**, 3865-3868.
48. J. P. Perdew, K. Burke and M. Ernzerhof, *Phys. Rev. Lett.*, 1997, **78**, 1396-1396.
49. P. E. Blochl, *Phys. Rev. B*, 1994, **50**, 17953-17979.
50. G. Kresse and D. Joubert, *Phys. Rev. B*, 1999, **59**, 1758-1775.
51. G. Kresse and J. Hafner, *Phys. Rev. B*, 1994, **49**, 14251-14269.
52. G. Kresse and J. Furthmuller, *Comp. Mater. Sci.*, 1996, **6**, 15-50.
53. O. Bludsky, M. Silhan, D. Nachtigallova and P. Nachtigall, *J. Phys. Chem. A*, 2003, **107**, 10381-10388.
54. O. Bludsky, M. Rubes, P. Soldan and P. Nachtigall, *J. Chem. Phys.*, 2008, **128**.
55. D. Nachtigallova, P. Nachtigall and O. Bludsky, *Phys. Chem. Chem. Phys.*, 2004, **6**, 5580-5587.
56. P. Nachtigall and R. Bulanek, *Appl. Catal. A-Gen.*, 2006, **307**, 118-127.
57. J. Kucera and P. Nachtigall, *Phys. Chem. Chem. Phys.*, 2003, **5**, 3311-3317.
58. C. O. Arean, O. V. Manoilova, M. R. Delgado, A. A. Tsyganenko and E. Garrone, *Phys. Chem. Chem. Phys.*, 2001, **3**, 4187-4188.
59. B. Bonelli, E. Garrone, B. Fubini, B. Onida, M. R. Delgado and C. O. Arean, *Phys. Chem. Chem. Phys.*, 2003, **5**, 2900-2905.

FIGURE CAPTION

Fig. 1 Structure of IPC-1PI, UTL, OKO and PCR consist of the same dense 2D layers (in green color) but different linkers (in red color) leading to the different pore sizes in these materials; shown for main channel (left side) and the perpendicular channel (right side).

Fig. 2 Notation used for extra-framework Li^+ cation sites in IPC-1PI, UTL, OKO and PCR. Sites in the main and perpendicular channels are denoted as M_x and P_x , respectively, where x stands for the size of the ring on the channel wall where the Li^+ cation is located. A new surface site in IPC-1PI formed upon the removal of D4R is denoted S8b. Two sites in PCR at the location of P5 and M5 in UTL are denoted M6 and P6 (insertion on the top). The numbering schemes of T' atoms following UTL numbering schemes are also shown.

Fig. 3 Powder XRD patterns (a) and adsorption-desorption isotherms of nitrogen measured at $-196\text{ }^\circ\text{C}$ (b) for UTL, OKO, and PCR zeolites and for 2D IPC-1PI pillared hierarchical material. The solid points denote desorption branch.

Fig. 4 FTIR spectra of CO adsorbed at liquid nitrogen temperature on Li-IPC-1PI (a), Li-UTL (b), Li-OKO (c), and Li-PCR (d). The intensity of spectra obtained upon CO adsorption decreases with evacuation. Insets in individual panels show theoretical spectra at corresponding Li-zeolites calculated for 0.75, 0.50, 0.25, 0.10, and 0.05 coverages (CO:Li ratio) in cyan, green, blue, red, and black, respectively.

Fig. 5 Adsorption heats of CO on Li-zeolites and Li-IPC-1PI measured by microcalorimetry at $-100\text{ }^\circ\text{C}$ as a function of coverage.

Fig. 6 The CO adsorption complexes in the most stable position of Li cation in IPC-1PI, UTL, OKO and PCR (from left to right); shown for Al in T4' (a-d); T3' (e-h); T10' (i-l) and T7' (m-p). The Al, O, and Si

atoms are depicted in black, grey, red and grey color, respectively while Li, C, and O atoms are depicted in purple, grey and red color balls, respectively.

Fig. 7 CO adsorption energies (lower part) and CO stretching frequencies (upper part) for the most stable Li^+ sites in IPC-1PI, UTL, OKO and PCR.

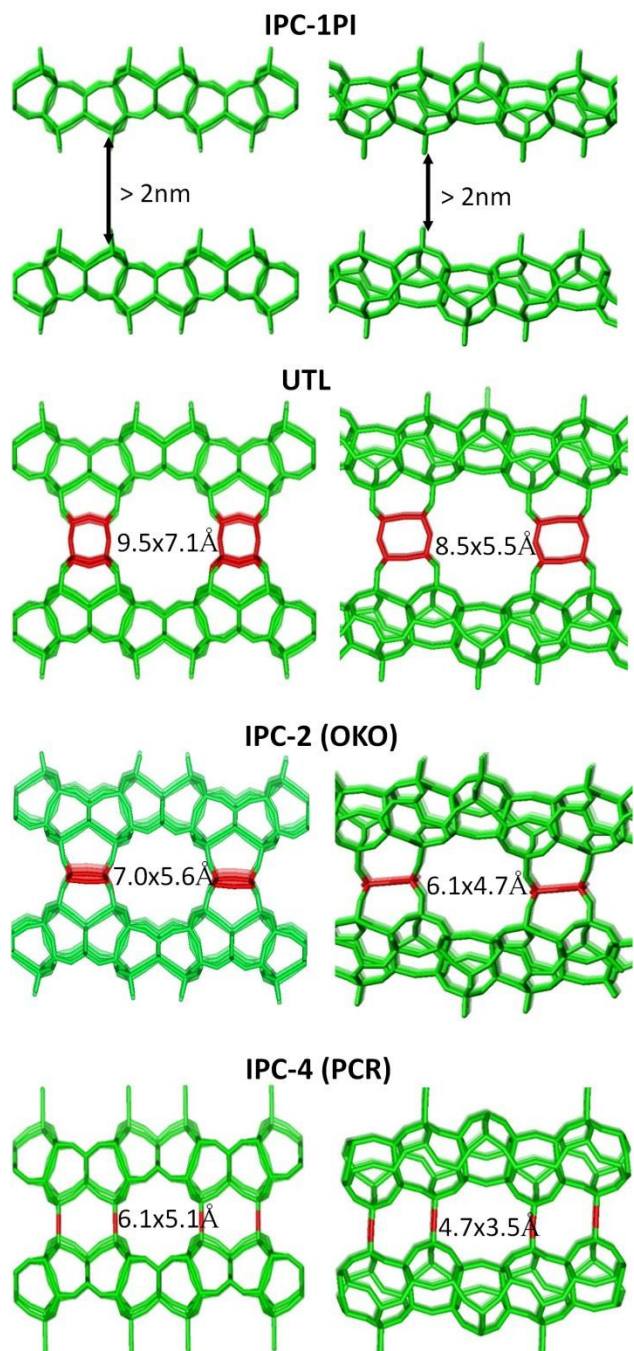


Fig. 1

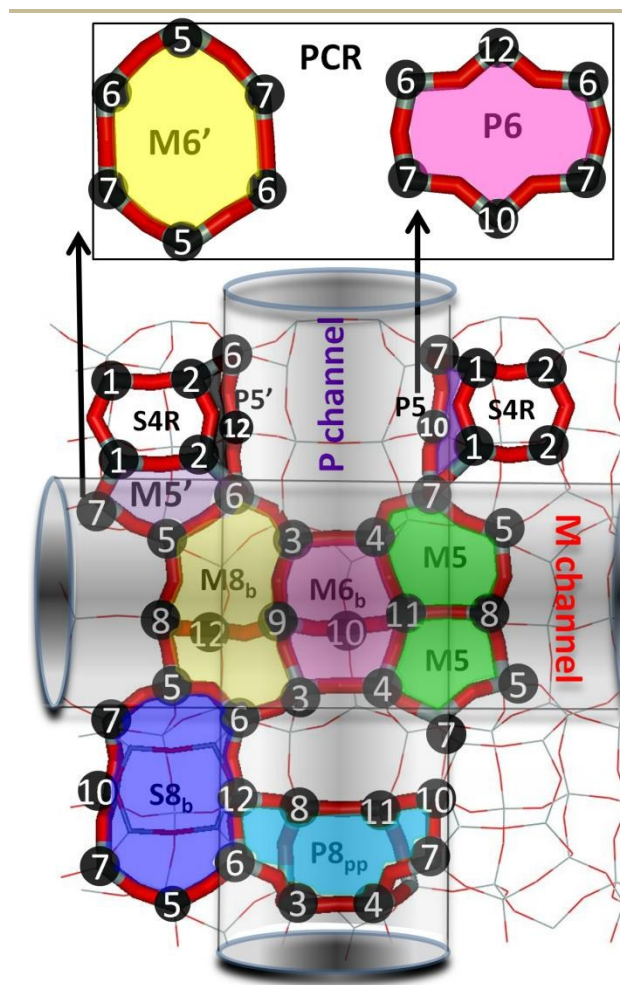


Fig. 2

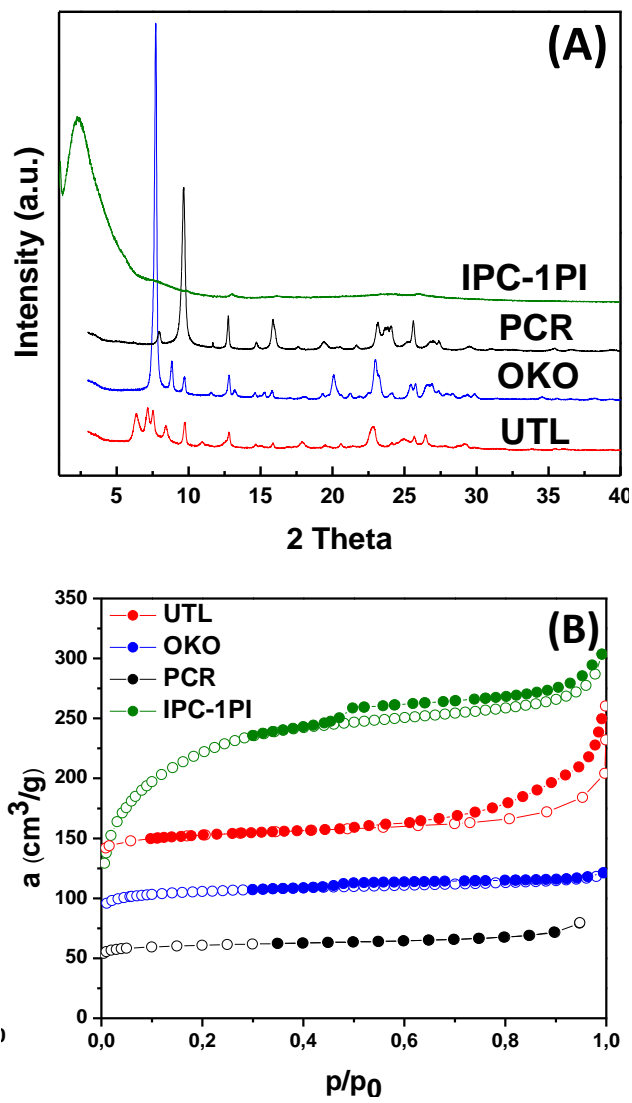
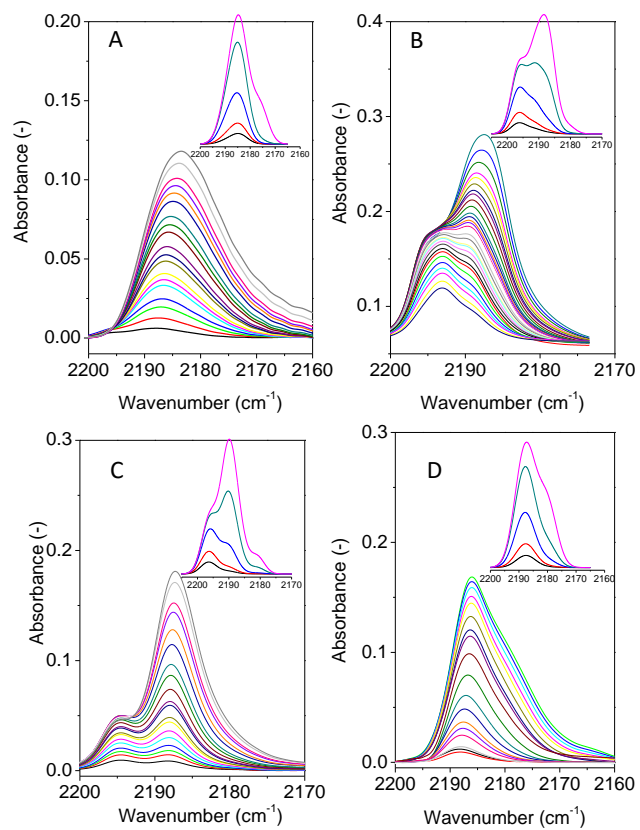


Fig. 3

**Fig. 4**

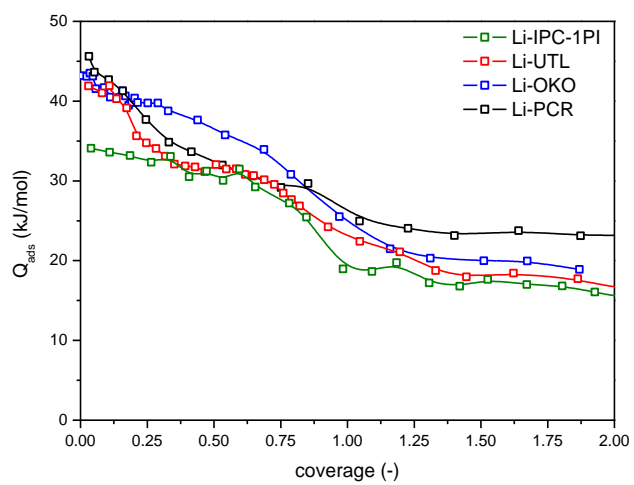
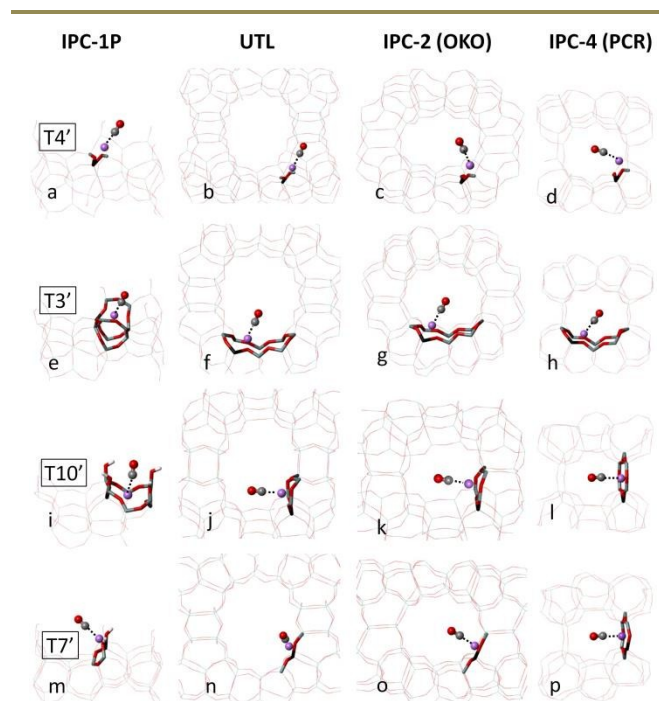


Fig. 5

**Fig. 6**

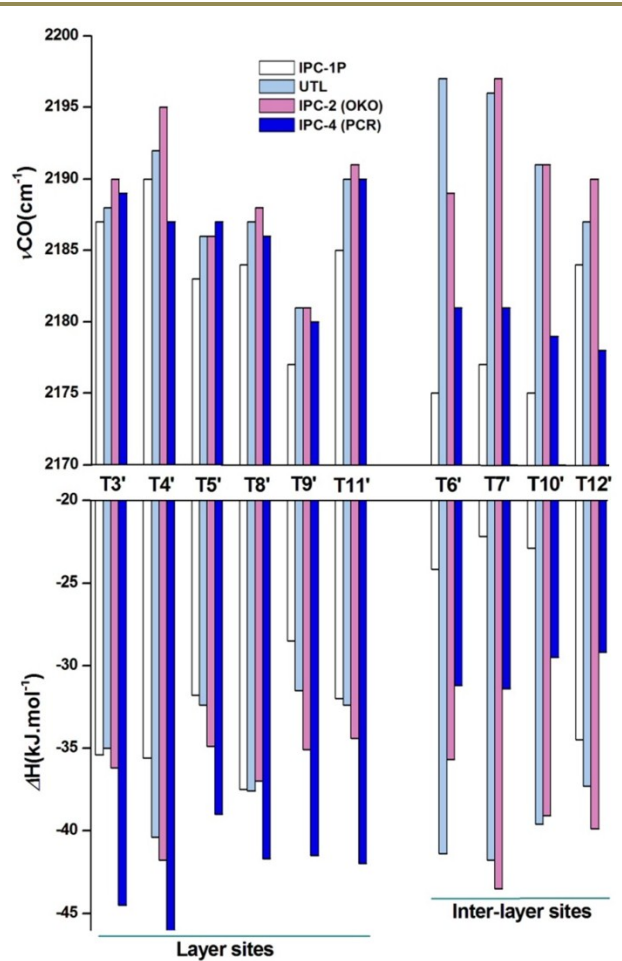


Fig. 7

Table 1 Textural properties determined by N₂ and Ar adsorption and chemical analysis of **UTL**, **OKO**, **PCR** and IPC-1PI zeolites.^a

Zeolite	Si/Al	N ₂ sorption			Ar sorption
		S_{BET}	V_{tot}	V_{micro}	Mean pore width
UTL	45	600	0.195	0.180	0.78
OKO	77	356	0.182	0.144	0.63
PCR	51	206	0.123	0.083	0.51
IPC-1PI	33	788	0.469	0.125	2.29

^a Surface area, volume and mean pore width are reported in m²g⁻¹, cm³g⁻¹ and nm, respectively

Table 2. Experimental and calculated CO adsorption characteristics for Li-IPC-1PI, Li-UTL, Li-OKO and Li-PCR.^a

zeolite	Q_{ads}^0 (exp.)	$-\Delta H$ (calc.)	ν_{CO} (exp.) ^b	ν_{CO} (calc.) ^b
Li-IPC-1PI	34.5	37	2187	2186
Li-UTL	41.0	42	2194; 2189	2196; 2188
Li-OKO	43.1	43	2195; 2188	2197; 2189
Li-PCR	44.0	46	2188	2188

^a Experimental adsorption heats estimates for zero coverage and a maximum $-\Delta H$ value calculated for particular system (in kJ mol^{-1}). ^b Frequencies (in cm^{-1}) taken from Fig. 4 for low coverage.

Table 3. The most stable Li⁺ cation positions, coordination numbers, distances to framework O_f atoms, adsorption heats and CO vibrational frequencies obtained computationally.^a

Al ^b location	Al ^b site	Li ⁺ cation position ^c (CN)		$r(\text{Li}\dots\text{O}_f)$		ΔH		ν_{CO}	
		OKO	PCR	OKO	PCR	OKO	PCR	OKO	PCR
<i>layer sites</i>	T3'	M8b(3)	M8b(3)	1.87, 2.02, 2.05	1.88, 2.10, 2.19	-36.2	-44.5	2190	2188
	T4'	I2(2)	I2(2)	1.86, 1.87	1.87, 1.89	-41.8	-46.5	2195	2187
	T5'	M8b(3)	M8b(3)	1.91, 1.94, 2.15	1.92, 1.93, 2.03	-34.9	-39.0	2186	2187
	T8'	M8b(3)	M8b(3)	1.93, 1.94, 2.03	1.94, 1.94, 2.10	-37.0	-41.7	2188	2186
	T9'	M8b(4)	M8b(4)	2.00, 2.05, 2.12, 2.13	1.98, 2.00, 2.12, 2.20	-35.1	-41.5	2181	2180
	T11'	M6b(3)	M6b(3)	1.95, 2.01, 2.32	1.97, 1.97, 2.31	-34.4	-42.0	2191	2190
<i>inter-layer sites</i>	T6'	M8b(3)	P6(4)	1.89, 2.01, 2.04	1.94, 2.06, 2.16, 2.24	-35.7	-31.2	2186	2181
	T7'	I2(2)	P6'(4)	1.87, 1.91	1.92, 2.10, 2.17, 2.20	-43.5	-31.4	2197	2181
	T10'	P5'(3)	P6'(4)	1.83, 2.01, 2.04	1.97, 1.97, 2.24, 2.24	-39.1	-29.5	2191	2179
	T12'	M8b(3)	P6(4)	1.89, 2.03, 2.09	1.96, 1.96, 2.16, 2.16	-39.9	-29.2	2190	2178

^a Distances, adsorption enthalpies, and frequencies reported in Å, kJ mol⁻¹, and cm⁻¹, respectively.

^b Al located either at the 2D dense layer (*layer sites*) or in the proximity of interlayer linker (*inter-layer sites*); for T-site numbering see Fig. 2 and Table SI-1.

^c See Fig. 2 for site notation; CN stands for number of O_f atoms at the distance of 2.4 Å or smaller from the Li⁺ cation.

Table 4. Summary of CO adsorption enthalpies and stretching frequencies for Li⁺ sites in Li-IPC-1PI, Li-UTL, Li-OKO, and Li-PCR.^a

Al location	Al site	ΔH				ν_{CO}			
		IPC-1PI	UTL	OKO	PCR	IPC-1PI	UTL	OKO	PCR
<i>layer sites</i>	T3'	-35.4	-35.0	-36.2	-44.5	2187	2188	2190	2188
	T4'	-35.6	-40.4	-41.8	-46.5	2190	2192	2195	2187
	T5'	-31.8	-32.4	-34.9	-39.0	2183	2186	2186	2187
	T8'	-37.5	-37.6	-37.0	-41.7	2184	2187	2188	2186
	T9'	-28.5	-31.5	-35.1	-41.5	2177	2181	2181	2180
	T11'	-32.0	-32.4	-34.4	-42.0	2185	2190	2191	2190
<i>inter-layer sites</i>	T6'	-24.2	-41.4	-35.7	-31.2	2175	2197	2189	2181
	T7'	-22.2	-41.8	-43.5	-31.4	2177	2196	2197	2181
	T10'	-22.9	-39.6	-39.1	-29.5	2175	2191	2191	2179
	T12	-34.5	-37.3	-39.9	-29.2	2184	2187	2190	2178

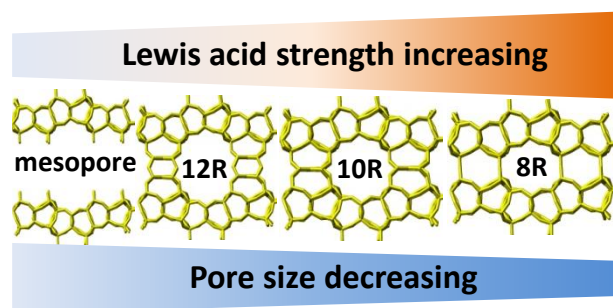
^a Adsorption enthalpies and frequencies reported in kJ mol⁻¹ and cm⁻¹, respectively.

Table 5. Average values of interaction energies (overall and its parts – dispersion and local contributions) and CO stretching frequencies.^a

	ΔH	Δ_{disp}	Δ_{local}	ν_{CO}
<i>layer sites</i>				
IPC-1PI	-33.5	-11.2	-22.3	2184.3
UTL	-34.9	-11.0	-23.9	2187.4
OKO	-36.6	-11.2	-25.4	2188.5
PCR	-42.5	-16.0	-26.6	2186.5
<i>inter-layer sites</i>				
IPC-1PI	-25.9	-7.8	-18.1	2177.7
UTL	-40.0	-10.5	-29.5	2192.8
OKO	-39.6	-11.0	-28.6	2191.8
PCR	-30.3	-15.7	-14.6	2179.8

^a Interaction energies and frequencies in kJ mol^{-1} and cm^{-1} , respectively. Values are averaged for *layer sites* and for *inter-layer sites*.

Graphical abstract



Lewis acid strength of Li^+ sites in Li-exchanged zeolites depends on the diameter of the pores.